

Geometric Data-Driven Multi-Jet Locomotion Inspired by Salps

Yanhao Yang, Nina L. Hecht, Yousef Salaman-Maclara, Nathan Justus, Zachary A. Thomas, Farhan Rozaidi, and
Ross L. Hatton

Abstract—Salps are marine animals consisting of chains of jellyfish-like units. Their capacity for effective underwater undulatory locomotion through coordinating multi-jet propulsion has aroused significant interest in the field of robotics and inspired extensive research including design, modeling, and control. In this paper, we conduct a comprehensive analysis of the locomotion of salp-like systems using the robotic platform “LandSalp” based on geometric mechanics, including mechanism design, dynamic modeling, system identification, and motion planning and control. Our work takes a step toward a better understanding of salps’ underwater locomotion and provides a clear path for extending these insights to more complex and capable underwater robotic systems. Furthermore, this study illustrates the effectiveness of geometric mechanics in bio-inspired robots for efficient data-driven locomotion modeling, demonstrated by learning the dynamics of LandSalp from only 3 minutes of experimental data. Lastly, we extend the geometric mechanics principles to multi-jet propulsion systems with stability considerations and validate the theory through experiments on the LandSalp hardware.

Index Terms—Calibration and Identification, Nonholonomic Motion Planning, Underactuated Robots, Biologically-Inspired Robots

I. INTRODUCTION

Salps are marine animals composed of chains of units¹ resembling open-ended, jellyfish-like tubes. These creatures are capable of efficient underwater undulatory locomotion by coordinating multi-jet propulsion. The structure and locomotion patterns of salps are closely related, which has attracted widespread interest in both biological and ecological research [1–5].

In the field of robotics, salps have attracted increasing attention due to their jet propulsion by expelling water through contraction, efficient underwater locomotion, and multi-unit coordination. Salps and jellyfish have inspired numerous robotic studies on the design of jet propulsion soft robots [6–12] and multi-robot coordination [13–17]. However, in the field of motion planning and control, most studies primarily consider undulatory locomotion by self-propulsion via body deformation [18–23], with only a few works involving underwater locomotion using jet propulsion [24–26].

This work was supported in part by ONR Award N00014-23-1-2171.

All the authors are with the Collaborative Robotics and Intelligent Systems (CoRIS) Institute at Oregon State University, Corvallis, OR USA. {yangyanh, Ross.Hatton}@oregonstate.edu

¹The units composing biological salps are called “zooids” (i.e., pseudoanimals or not-quite-animals) because they exhibit many properties of animals but are not independent organisms from the colony. To discuss the general properties of multi-jet locomotion without making claims about the biological systems that inspire them, we use the terminology “chains” and “units” throughout this paper.

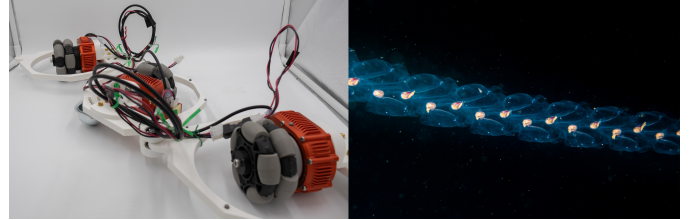


Fig. 1. The LandSalp robot and sea salps. The salp picture is reproduced from [27].

Although robotics research on salps exists, most studies focus only on single aspects of their underwater locomotion, often neglecting other couplings in the locomotion [6–12]. For example, while numerous designs of soft actuator-based jet propulsion mechanisms have successfully reproduced biological behaviors, few studies have specifically considered the relationship between the unit arrangement and locomotion patterns of such multi-jet robots and their corresponding control. When multiple jet propulsion mechanisms form a chain of salps, coordination and control become critical for effective and efficient locomotion.

Further, in many studies focused on underwater locomotion, it is typically assumed that system control forces are aligned with internal shape degrees of freedom, such that the system’s shape can be directly controlled, and then shape-change patterns can be identified to efficiently propel the system by pushing against the environment [18–23]. However, the jet forces produced by salps project into both the shape and position directions, meaning that the control of these quantities cannot be easily decoupled [24–26]. Coupled shape/position locomotion introduces new challenges in motion planning and control, which requires considering both the system’s locomotion and the stability of the system’s shape during locomotion. This consideration is particularly critical when implementing motion planning and control algorithms in hardware.

Additionally, in many multi-agent coordination studies, it is typically assumed that each agent has low-level control over instantaneous omnidirectional locomotion [13–17]. However, for a jet-propelled underwater locomotion system, such instantaneous omnidirectional control authority is not always guaranteed, and the stability of the coupled shape/position locomotion must also be considered.

In this paper, we use geometric mechanics to reduce the complex, high-dimensional locomotion of salp-like systems to a compact, low-dimensional system for design, analysis, and planning. Historically, geometric mechanics has been a power-

ful tool for analyzing locomotion, with applications across various robotics disciplines such as design [28], modeling [21,29], system identification [29–31], and motion planning [22,23]. Geometric mechanics unifies the modeling of a wide range of nonholonomic locomotion types through local metrics [32], including swimming at low and high Reynolds numbers [21], terrestrial wheel-driven motion [33], and self-reorientation in space [34]. Building on these insights, we extract the key physical principles underlying the underwater locomotion of salps, develop an efficient data-driven methodology to learn the Riemannian metric characterizing their dynamics from minimal experimental data, and extend existing geometric motion planning methods previously applied to directly controllable shapes to account for the jet propulsion dynamics of salps.

This paper presents a comprehensive study of the locomotion of salps, including mechanism design, dynamic modeling, system identification, motion planning, and feedback control. We also developed a land-based robotic platform “LandSalp”, as an extension of previous work [35]. This platform can reproduce the key features of underwater locomotion of salps on land, enabling us to evaluate our approach with minimal confounding factors. The research contributes to a deeper understanding of salps’ underwater locomotion, offering a foundation for advancing these insights to more complicated and capable underwater robotic systems. More broadly, this work demonstrates the power of geometric mechanics in the design, modeling, and control of bio-inspired robots and validates the theory using LandSalp hardware. Specifically, the contributions of this work are as follows:

- 1) The combination of geometric motion planning and averaging theory to adapt force-controlled systems that necessitate stability consideration and feedback control, with application to multi-jet underwater locomotion.
- 2) The design and construction of the “LandSalp” robot based on the geometric mechanics model, whose dynamics are essentially similar to those of multi-jet swimming of salps;
- 3) An efficient data-driven locomotion modeling method based on geometric mechanics that accurately characterizes the dynamics of LandSalp with minimal experimental data; and

Based on the proposed data-driven geometric modeling approach, we successfully developed an accurate dynamic model of the LandSalp robot with only about 3 minutes of experimental data. Utilizing this model, we applied the proposed geometric motion planning and feedback control algorithms to demonstrate the omnidirectional locomotion of LandSalp in both simulated environments and physical hardware.

II. GEOMETRIC MODELING FOR UNDERWATER LOCOMOTION OF SALPS

In this section, we propose a geometric mechanics model for salp locomotion based on low Reynolds number dynamics with jet forces. Based on this model, we analyze salps with linear-like architectures and derive the control vector field that maps jet force controls to the system’s configuration velocities.

TABLE I
KEY SYMBOLS USED THROUGHOUT THIS PAPER

Symbol	Meaning
$\alpha, \dot{\alpha}$	Individual joint positions and velocities
r, \dot{r}	System shape and shape velocity
g, \dot{g}	System position and body velocity
q, \dot{q}	System configuration and its (group) derivatives
w^{jet}, u	Controlled jet force and controlled jet velocity
f, τ	Forces and moments expressed in the system’s body frame and joint torques
\tilde{f}	Force measurement from the series-elastic actuator
f_q	Total forces and moments pulled back to the system configuration coordinates
$d^{\text{unit}}, d^{\text{joint}}, D$	Salp unit drag coefficient (expressed in local body coordinates), joint viscous friction coefficient, and the aggregate drag coefficient matrix
J_i	Jacobian matrix mapping system configuration velocities to the body velocity of the i -th salp unit
J_q, J_u	Jacobians mapping configuration velocity and controlled jet velocity, respectively, to the body velocity of the salp units and joints, where viscous drag occurs and drag coefficients are defined
J_{f_q}, J_{f_u}	Jacobian matrices mapping system drag coefficients to total forces and moments in system configuration coordinates and series-elastic actuator directions
B	Control vector field
S	Selection matrix extracting the force component aligned with the series-elastic actuator
h	Rigid body transformation within the system
λ	Regularization strength
$\bar{u}, A^{\text{sin}}, A^{\text{cos}}$	Fourier series constant and oscillation coefficients
\tilde{u}	Control parameters
T, ω	Gait period and frequency
R	Gait cost metric
K	Feedback gains
$(\cdot)^{\text{aug}}$	Augmented terms with Lie brackets accounting for gait cycle effects
$(\cdot)^{\text{desired}}$	Desired motion for control

Biological analysis of salps indicates that they swim at relatively low Reynolds numbers [4]. This condition allows us to reasonably model the underwater locomotion of salps as being dominated by viscous drag, with any inertial effects immediately damped out [21].² This model has two consequences for our system analysis:

- 1) The drag on each salp unit is a linear function of its body velocity, which can be pulled back to be a linear function of the body and shape velocity of the entire system; and
- 2) An isolated salp chain is in quasi-static equilibrium: the net drag forces and moments from its interaction with the surrounding fluid and joint frictions are equal and opposite to the forces and moments induced by the jet.

The first consequence of the low Reynolds number assumption (linear drag) allows us to rewrite the total force and moment on each salp unit as:

$$f_i = w_i^{\text{jet}} - d_i^{\text{unit}} \circ g_i, \quad (1)$$

where the subscript i denotes the i -th salp unit, and all terms

²To extend the proposed methods beyond this assumption, please refer to [23] for an inertia-dominated kinematic model, and to [36] for a dynamic model that considers both the inertial and drag effects on the body as well as the spring stiffness at the joints.

are expressed in that unit's body frame:³ f_i represents the total force and moment on the unit, u_i^{jet} denotes the jet force, d_i^{unit} is the drag coefficient matrix, and \dot{g}_i represents the body velocity of the unit. Furthermore, by normalizing the jet force with the drag coefficient, we define the controlled jet velocity for propulsion as:

$$u_i = (d_i^{\text{unit}})^{-1} u_i^{\text{jet}} \quad (2a)$$

$$f_i = d_i^{\text{unit}} (u_i - \dot{g}_i), \quad (2b)$$

where u_i is the controlled jet velocity of jet propulsion.⁴ This formulation makes it possible to simulate the underwater locomotion of sea salps in a physically equivalent manner using the LandSalp robot with series-elastic actuators.

Similarly, we also model the viscous friction on each joint as being proportional to its rotational velocity:

$$\tau_j = -d_j^{\text{joint}} \dot{\alpha}_j, \quad (3)$$

where the subscript j denotes the j -th joint, and all terms are expressed in the generalized coordinates of the j -th joint: τ_j represents the viscous friction on the joint, d_j^{joint} is the drag coefficient, and $\dot{\alpha}_j$ represents the joint velocity.

Given the representation of the force on each salp unit and the drag on each joint, the second consequence of the low Reynolds number assumption (quasi-static equilibrium) provides the nonholonomic constraints for determining the system motion based on the controlled jet force. These nonholonomic constraints can be expressed as the condition that the total force and moment applied to the system configuration coordinates sum to zero:

$$f_q = \begin{bmatrix} f_o^T & f_r^T \end{bmatrix}^T \quad (4a)$$

$$= \sum_i^n J_i^T f_i + \begin{bmatrix} \mathbf{0} \\ \boldsymbol{\tau} \end{bmatrix} = \mathbf{0} \quad (4b)$$

where J_i is the Jacobian that maps the configuration velocity to the body velocity of the i -th salp unit, and its transpose maps the forces acting on the salp unit back to the configuration coordinates. The term f_q includes the net force and moment applied to the system's body frame, as well as the total moment acting on the joints. Specifically, this term is computed by pushing forward the total forces and moment on each salp unit, f_i , using the corresponding Jacobians and incorporating the effects of viscous friction at each joint, $\boldsymbol{\tau}$. Next, we define the specific configuration and derive the Jacobians based on the system's kinematics.

In this paper, we will focus on the planar motion of salps with linear-like architectures⁵ [37], as shown on the right side

³The "open circle" notation we use here is similar to the "dot" notation, but denotes derivatives with respect to group actions rather than coordinate values. Please refer to Appendix A for more details.

⁴In this paper, the series-elastic actuators on the robot, which simulate the combined water jet and viscous drag, can only be controlled by accessing the jet velocity u . Therefore, in the following sections, we will use the jet velocity for our derivations. However, our approach can be directly generalized to scenarios where thrusters or propellers are controlled with direct access to the jet force u^{jet} .

⁵It is important to highlight that the same modeling methodology is applicable to salps with other architectures and exhibiting three-dimensional motion.

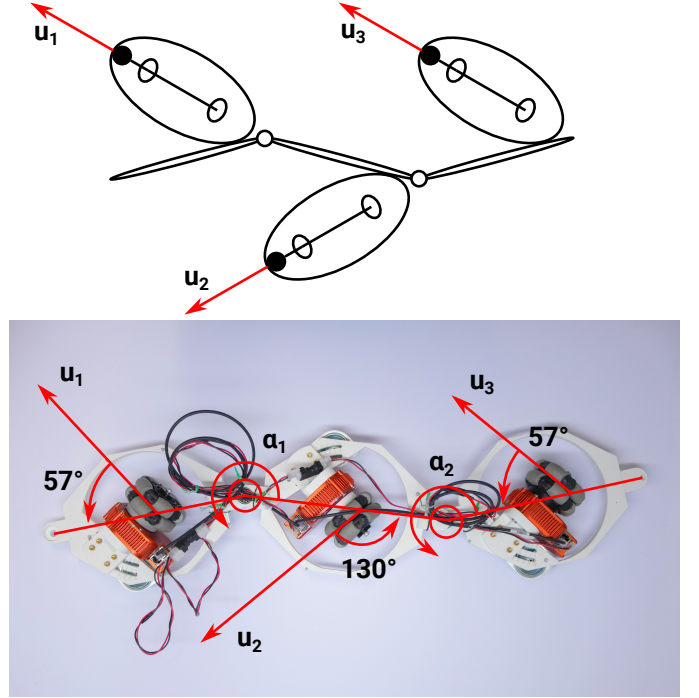


Fig. 2. Schematic comparison of the LandSalp robot and the corresponding sea salp with linear-like architectures. There are two joints connecting the links from left to right. The orientations of the three motor-wheel assemblies used to generate jet thrust and viscous drag are -57° , -130° , and -57° , respectively, from left to right, relative to the link axis.

of Fig. 1. Salp-like linear chain with n units can be modeled as chains of n links with $n - 1$ passive joints between the links and n water jets alternating in different directions on each link, as shown on the upper side of Fig. 2. In this model, the control input is the jet velocity u , and the passive configuration velocity can be decomposed⁶ into the body velocities⁷ of the system \dot{g} and shape (joint) velocities \dot{r}

$$u = \begin{bmatrix} u_1 \\ \vdots \\ u_n \end{bmatrix} \quad \dot{r} = \begin{bmatrix} \dot{\alpha}_1 \\ \vdots \\ \dot{\alpha}_{n-1} \end{bmatrix} \quad \dot{q} = \begin{bmatrix} \dot{g} \\ \dot{r} \end{bmatrix}. \quad (5)$$

The body velocity of each salp unit, \dot{g}_i , can be computed from the configuration velocity using differential kinematics, given the transformation from the system body frame to the frame of the i -th salp unit $h_i(r)$ and the transformation from the j -th joint to the i -th salp unit $h_{\frac{i}{j}}(r)$

$$\dot{g}_i = Ad_{h_i}^{-1} \dot{g} + \sum_{j=1}^{i-1} Ad_{h_{\frac{i}{j}}}^{-1} \begin{bmatrix} 0 \\ 0 \\ \dot{\alpha}_j \end{bmatrix} \quad (6a)$$

$$= J_i \dot{q}, \quad (6b)$$

⁶Formally, this decoupling is embodied in a differential geometric structure called a *fiber bundle*, where the *shape* and *position* of the system are respectively referred to as elements of the *base* and *fiber* spaces [38].

⁷To improve accuracy and better represent the robot as a whole, we use a body frame defined by the center of mass and the mean orientation of each link [39]. For a more detailed discussion on the choice of coordinates that define the system, please refer to Appendix D.

where J_i is the Jacobian that maps the configuration velocity to the body velocity of the i -th salp unit and Ad is the adjoint operator.⁸

The total forces and moments acting on the salp system include the viscous drag on each salp unit and joint, as well as the active water jet force on each salp unit. These forces and moments can all be mapped to the configuration coordinates using the corresponding Jacobians, resulting in the force balance equation given in (4b):

$$f_q = \sum_i^n J_i^T d_i^{\text{unit}} (u_i - \dot{g}_i) - \begin{bmatrix} \mathbf{0} \\ d_1^{\text{joint}} \dot{\alpha}_1 \\ \vdots \\ d_{n-1}^{\text{joint}} \dot{\alpha}_{n-1} \end{bmatrix} \quad (7a)$$

$$= J_q^T D [J_q \quad J_u] \begin{bmatrix} \dot{q} \\ u \end{bmatrix}, \quad (7b)$$

where J_q and J_u are the Jacobians that map the configuration velocity and the controlled jet velocity, respectively, to the body velocity of the salp units and the joints where viscous drag occurs and the drag coefficients are defined. D denotes the aggregated local metrics, represented as a block diagonal matrix that contains the drag coefficients for each salp unit and joint. By setting the total forces and moments on the configuration coordinates to zero, one can solve the system's equation of motion [32]

$$\dot{q} = - \underbrace{(J_q^T D J_q)^{-1} J_q^T D J_u}_{B} u \quad (8)$$

where B is the control vector field that maps control to the body and shape velocity of the system. Fig. 3 illustrates the control vector fields of the LandSalp robot we designed to emulate the underwater locomotion of salps. The following section discusses this design in detail.

III. LANDSALP DESIGN FOR SIMULATING UNDERWATER LOCOMOTION OF SALPS

Considering that the underwater locomotion of salps is dominated by viscous drag, the total force and moment exerted on each salp unit are directly proportional to the difference between the controlled jet velocity and the salp unit's body velocity, as demonstrated in (2b). This relationship allows us to design the LandSalp robot, which leverages the precise force control of series-elastic actuators, to replicate the underwater locomotion of salps in a physically equivalent way on a flat table surface without the testing overhead of aquatic operations. This robot allows us to establish our modeling and control strategies with a minimum of confounding factors, while also providing a clear development pathway for extending these strategies to more complicated and capable swimming systems.

The LandSalp is constructed as a planar chain of links connected by passive joints, as illustrated on the left side of Fig. 1 and on the bottom side of Fig. 2. As illustrated

⁸The adjoint operator Ad_{\bullet} combines the cross-product operation—which converts linear and angular velocities or forces/momenta between different frames—with the rotation operation that expresses velocities or forces/momenta in body-aligned coordinates.

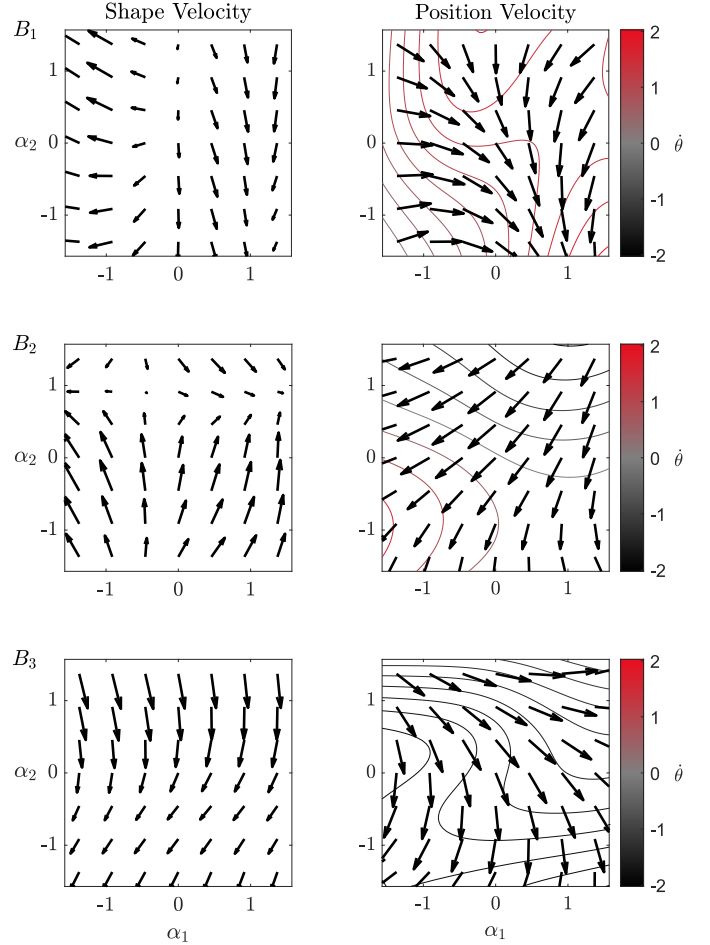


Fig. 3. Control vector fields B for the LandSalp data-driven model. Each row corresponds to each control input. The left column shows the shape velocity resulting from each control input at different shapes, and the right column shows the position velocity resulting from each control input at different shapes, with the linear velocity in the \hat{x} and \hat{y} directions overlaid with the shape axes, and the contours showing the angular velocity $\dot{\theta}$.

TABLE II
SPECIFICATIONS OF LANDSALP

Parameter	Value
Link Length (m)	0.27
Omn wheel Diameter (m)	0.083
Omn wheel Orientation(deg)	-57, -130, -57
Actuator Maximum Speed (RPM)	32, 14, 32
Actuator Continuous Torque (Nm)	4, 8, 4

in Fig. 4, each link is equipped with a HEBI series-elastic actuator driving an omn wheel, and has a ball-caster acting as a balance support, ensuring that the links remain in the horizontal plane. Each of these links forms a unit in our LandSalp robot (corresponding to the zooids in a biological salp), with the motor-omn wheel assemblies simulating the water jet propulsion and viscous drag.

The motor-omn wheel assemblies are individually controlled such that their output torque is a combination of a commanded driving torque and a drag term that simulates fluid drag acting on the link as it moves. In addition, viscous friction arises from the omn wheel rollers, the wheel steering,

the ball caster motion, and the joint rotations. Notably, the robot's actuation and drag closely mimic the force distribution observed in salps, where the net forces comprise both the water jet force and viscous drag.

Furthermore, the constrained joint angles require the motors to operate the wheels in a cyclical and reciprocating fashion - referred to as a gait in Section V - to propel the robot, which essentially simulates the pulsating intake and ejection of water observed in salps.⁹ These assemblies can be placed at different orientations relative to the link by being mounted in different positions of the rotation slot, corresponding to different orientations of the jets on a salp relative to its body. For the following studies and experiments, we mounted the three omniwheels at -57° , -130° , and -57° relative to the link axis. Table II shows the main specifications of the LandSalp robot. It is noteworthy that a different motor module is employed on the center link, which has approximately half the maximum speed and twice the torque limit compared to the motors on the side links.

Once the kinematics are updated according to the dimensions of LandSalp, all geometric modeling of the underwater locomotion of salp derived from (4b) can be applied to LandSalp, again demonstrating the physical equivalence of the LandSalp locomotion and the underwater locomotion of the sea salps. This equivalence allows us to validate the proposed modeling and control strategies on LandSalp with minimal confounding factors and demonstrates the feasibility of extending these strategies to underwater robots.

IV. DATA-DRIVEN GEOMETRIC MODEL IDENTIFICATION

Although we have established a geometric model of the underwater locomotion of salps based on viscous drag, the drag coefficients encoding this model remain undetermined. Fortunately, the geometric modeling method proposed above provides an efficient data-driven geometric model identification method to learn these coefficients from experimental data. In this section, we will use LandSalp as an example to demonstrate the data-driven geometric model identification method.

A. Data Collection

For data collection, we used the OptiTrack motion capture system to record the motion of each link of the LandSalp,¹⁰ from which the system's position and joint angles were calculated. System velocities were obtained by applying Lie-group

⁹Note that in this paper, we assume that the LandSalp robot is capable of bidirectional wheel actuation. As discussed in [3], salps have incurrent and excurrent siphons at opposite ends of their bodies, enabling reverse swimming—albeit with different efficiencies. Future work will explore unidirectional jet propulsion, which poses additional control challenges due to its inherent limitations in instantaneous controllability. Such limitations may be overcome by implementing a cyclic gait, as discussed in Section V.

¹⁰In this paper, we use motion capture to record the robot's motion relative to the world for a more intuitive demonstration. However, it is important to emphasize that the proposed method is not limited to this. If a state estimator can be implemented using onboard inertial measurements [40], our method is capable of learning coefficients exclusively from proprioceptive data.

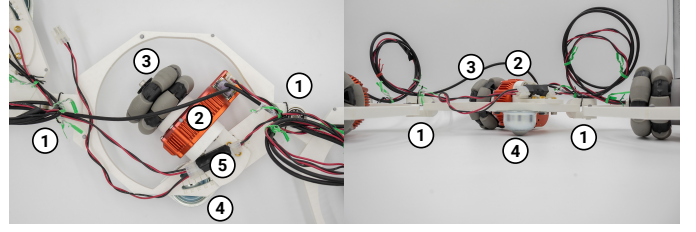


Fig. 4. The LandSalp is constructed as a planar chain of links, each link consisting of the following components: 1) passive joints, 2) HEBI X5 series-elastic actuators, whose output torque is a combination of a commanded driving torque and a drag term that simulates fluid friction acting on the link as it moves, 3) omniwheels, 4) ball casters for balancing, 5) rotation mounting slots for adjusting wheel orientation to correspond to different jet directions.

time differentiation to the position data.¹¹ The driving torque was obtained from the torque sensing of the series-elastic actuator. The motion capture data was sampled at a frequency of 240 Hz, and the series-elastic actuator data was sampled at 200 Hz. All measurements were resampled to 200 Hz for subsequent unified processing. Additionally, all collected data were low-pass filtered to reduce noise.

When conducting the data collection experiments, we alternated the driving direction of each omniwheel and exhausted all possible driving combinations of the three wheels, so that the collected data could fully cover all possible couplings between the links. We recorded 8 runs in different orders and directions, making up a total of about 3 minutes of data. The input command was a constant frequency sine wave of 1/6 Hz, which is designed based on the actuator's maximum velocity and the omniwheel's maximum traction on the flat surface. Considering the proposed viscous drag-based model is first-order, the cutoff frequency of the low-pass filter was set according to the command frequency.

B. Data-Driven Local Metrics

As demonstrated in (7b), the actuation and viscous drag on each unit and joint can be pulled back to the configuration coordinates. Notably, the total configuration forces and moments are linear functions of the aggregated local metric D

$$f_q = J_q^T D \begin{bmatrix} J_q & J_u \end{bmatrix} \begin{bmatrix} \dot{q} \\ u \end{bmatrix} \quad (9a)$$

$$= \underbrace{\left(\begin{bmatrix} J_q & J_u \end{bmatrix} \begin{bmatrix} \dot{q} \\ u \end{bmatrix} \right)^T \otimes J_q^T}_{J_{f_q}} \text{vec}(D), \quad (9b)$$

where \otimes is the Kronecker product and $\text{vec}(\cdot)$ is the vectorization operation [41]. Similarly, by rewriting (2b), the force and moment acting on each individual salp unit, as well as its

¹¹Lie-group time differentiation is analogous to standard time differentiation, but it computes derivatives with respect to group actions rather than changes in coordinate values. For further details, please refer to Appendix A.

component in the direction of the series-elastic actuator, can be expressed as linear functions of the local metric, D :

$$S \begin{bmatrix} f_1 \\ \vdots \\ f_n \end{bmatrix} = SD \begin{bmatrix} J_q & J_u \\ \dot{q} \\ u \end{bmatrix} \quad (10a)$$

$$= \underbrace{\left(\left(\begin{bmatrix} J_q & J_u \\ \dot{q} \\ u \end{bmatrix} \right)^\top \otimes S \right)}_{J_f} \text{vec}(D), \quad (10b)$$

where S is the selection matrix that extracts the force component aligned with the series-elastic actuator.

Given the quasi-static equilibrium of the viscous drag-dominated system, as in (4b), the total force and moment on the system are balanced, i.e. $f_q = 0$. Furthermore, the total net power on the system is also zero, i.e. $\langle f_q; \dot{q} \rangle = 0$. In addition, as shown in (2b), the force applied to each salp unit, f_i , in the direction aligned with the series-elastic actuator, should correspond to the torque sensing of the series-elastic actuator. These relationships enable an efficient data-driven modeling approach by leveraging motion capture data and the torque sensing of the series-elastic actuator.

Specifically, the data-driven geometric model identification can be formulated as a semidefinite program that minimizes the difference between the model-predicted forces and the experimental data for a given locomotion, while regularizing the model using the zero total net power condition from the low Reynolds number swimming regime

$$\min_D \left\| J_f \text{vec}(D) - \begin{bmatrix} \tilde{f}_1 & \cdots & \tilde{f}_n \end{bmatrix}^\top S^\top \right\|_2^2 + \lambda \langle J_{f_q} \text{vec}(D), \dot{q} \rangle \quad (11a)$$

$$s.t. \quad D \succeq 0 \quad (11b)$$

$$D \text{ is a diagonal matrix} \quad (11c)$$

where λ is the strength of the regularization, and \tilde{f}_i denotes the force measurement from the series-elastic actuator. The objective function is designed to learn the drag coefficient from torque sensing while ensuring that the system dynamics satisfy the low Reynolds number swimming condition. The first constraint guarantees that the local metric tensor is positive definite, and the second constraint ensures our assumptions that drag occurs only on each wheel and joint independently and that the drag on the wheel is aligned with its principal axis.¹² In practice, we follow the approach in [42] to make the problem coordinate-independent by first solving the unregularized problem and then using the error covariance to rescale the objective function.

Fig. 5 shows the data-driven local metrics learned from experimental data and the corresponding residual gradients for each entry. The results are consistent with our intuition that the main driving force comes from drag in the direction of wheel rotation. Furthermore, the friction model accounts for extra

¹²Modeling only the diagonal terms makes the model more robust and less prone to overfitting to limited data, but more coupled effects can be modeled if necessary when the rank (i.e., observability) of the data matrix is sufficient.

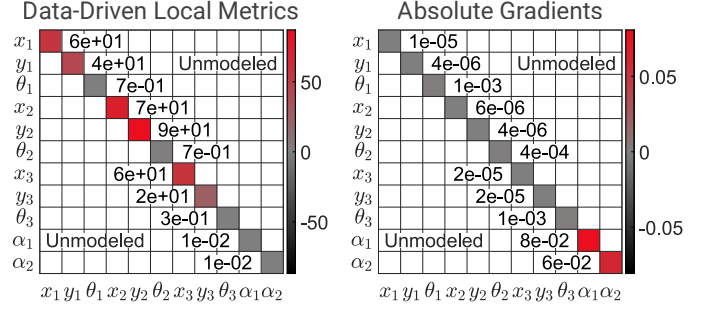


Fig. 5. Data-driven local metrics and corresponding residual gradients. In this paper, we assume that the drag of the wheels and joints is independent, and the principal axes of the local metric are aligned with the wheels. The white grids are unmodeled entries.

viscous effects arising from the rolling of the omnivheel's rollers, the steering of the wheels, the rolling resistance of the ball casters, and the rotation of the joints. It is important to note that the drag coefficients here are specific to their associated velocities, resulting in different units and scales when comparing linear drag to rotational drag.

The large drag observed on the y-axis of the center wheel is likely due to the unmodeled inertia effect, specifically the force necessary to open or close the two side links when moving in the rolling direction of the center wheel. The residual gradients are small overall, indicating the stability of the data-driven model. The relatively high sensitivity in the drag of the two joints and the rotational drag of the wheels is due to the differing scales and units compared to the linear drag on the wheels.

It is important to highlight that the data-driven geometric model identification method is not limited to systems dominated by viscous drag. In principle, any locomotion system that can be modeled via Riemannian metrics can be similarly identified, provided that sufficient sensor data is available. As envisioned in Section VII, our methodology is generalizable to systems operating at intermediate Reynolds numbers, which requires consideration of both inertial and drag effects, as well as joint stiffness. This finding shows the potential of our method to generalize across a wide range of environments and locomotion scenarios.

V. GEOMETRIC MOTION PLANNING AND CONTROL

Once the model coefficients have been determined through data-driven geometric model identification, we can proceed to consider motion planning and control of salps. However, this task is not straightforward for two reasons:

- 1) The control vector field B indicates that it is impossible to directly and instantaneously control all passive states of the system through linear combinations of control inputs. This limited instantaneous control authority requires the use of oscillatory inputs, which aim to achieve control of all passive states of the system through periodic control inputs within specific actuation limits.
- 2) Unlike the systems in extensive prior work on undulatory locomotion that assume direct shape control [18,19,21–24], salps achieve locomotion via reaction forces from

water jets. These force-controlled systems require additional stability considerations because the shapes, which have inherent limits and influence the control vector field, cannot be directly controlled.

To address these issues that distinguish salps from conventional bio-inspired robotic systems, in this section, we will explore the application of geometric mechanics, averaging theory, and Lie group theory for geometric motion planning and feedback control of LandSalp to achieve omnidirectional locomotion and maintain stability.

Specifically, this section will focus on the gait analysis and optimization of LandSalp. Gaits, commonly observed in animals such as horses running, humans walking, and snakes swerving, not only elevate controllability analysis from an instantaneous to a periodic level, but also better represent the water loading and ejection processes of salps.

A. Controllability and Gait Analysis

Given that the control vector field for an n -link salp is a $(2+n)$ -by- n matrix (5-by-3 for LandSalp), it is not feasible to achieve direct control over all passive components of the system instantaneously through linear combinations of control inputs. Here, we will analyze the system's controllability by extending the control authorities using first-order Lie brackets for oscillatory control inputs.

Given the limited range of joint motion and the maximum velocity of the actuators, we use a periodic gait as the control input. A gait can be parameterized as a Fourier series¹³ consisting of a constant component \bar{u} and k -th order oscillatory components determined by amplitudes $A^{\sin,k}$ and $A^{\cos,k}$ and a baseline frequency ω ¹⁴

$$u(t) = \bar{u} + \sum_{k=1}^{\infty} (A^{\sin,k} \sin(2k\pi\omega t) + A^{\cos,k} \cos(2k\pi\omega t)). \quad (12)$$

The LandSalp locomotion resulting from executing this gait around a nominal shape r^{nominal} during a gait cycle can be expressed as a Baker-Campbell-Hausdorff (BCH) series and averaged using averaging theory. In this formulation, the geometrically averaged velocity $\dot{q}^{\text{avg}} \in \mathfrak{se}(2) \times \mathbb{R}^m$ (the constant body and shape velocity that produces the net displacement observed over the gait cycle) is obtained by taking the logarithm of the net displacement, $q(T) \in SE(2) \times \mathbb{R}^m$, divided by the cycle period, $T = 1/\omega$. The net displacement is represented as the continuous product of the exponentials

¹³Physically, the periodic components in this context can be interpreted as cyclic variations in flow or force in the water jet cycle, and the constant component corresponds to the average flow through the jet.

¹⁴Taking into account the actuator's maximum speed limit, the wheel's maximum traction on a flat surface, and the approximate accuracy of truncation at the first-order Lie bracket, we have manually selected a control frequency as 1/6 Hz in this paper.

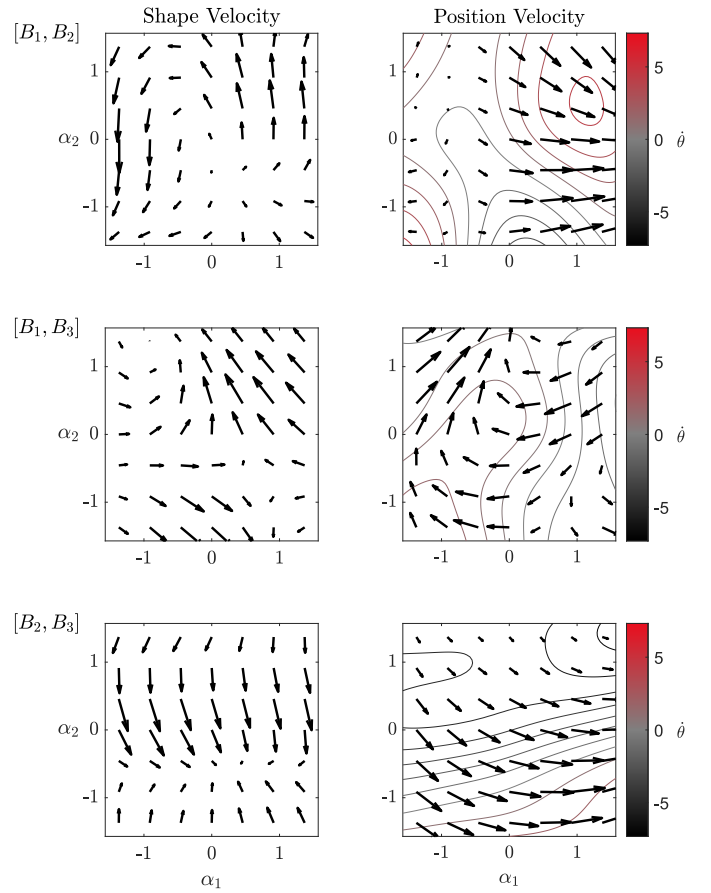


Fig. 6. First-order Lie brackets of the control vector fields for the LandSalp data-driven model. The left column shows the shape velocity results for each Lie bracket pair at different shapes, and the right column shows the position velocity results for each Lie bracket pair at different shapes, with the linear velocity in the \dot{x} and \dot{y} directions overlaid with the shape axes, and the contours showing the angular velocity $\dot{\theta}$.

corresponding to all of the input responses:

$$\dot{q}^{\text{avg}} = \frac{1}{T} \log q(T) \quad (13a)$$

$$= \frac{1}{T} \log \left(\prod_0^T \exp(Bu(t)dt) \right) \quad (13b)$$

$$= \frac{1}{T} \int_0^T Bu(t)dt + \frac{1}{T} \int_0^T \int_t^T \frac{1}{2} [Bu(t), Bu(\tau)] d\tau dt + \dots \quad (13c)$$

$$\approx \frac{1}{T} \int_0^T Bu(t)dt + \frac{1}{T} \int_0^T \int_t^T \frac{1}{2} [Bu(t), Bu(\tau)] d\tau dt \quad (13d)$$

$$= B\bar{u} + \sum_{i=1}^m \sum_{j=i+1}^{m+1} \frac{1}{2\pi\omega} u_{[i,j]} [B_i, B_j], \quad (13e)$$

where we first express (13b) as a BCH series as demonstrated in (13c) [43,44], then truncate it at the first-order Lie bracket as shown in (13d), and finally integrate the controlling Fourier series form as presented in (13e). $[B_i, B_j]$ represents the Lie

bracket of the control vector fields B_i and B_j , and $u_{[i,j]}$ denotes the corresponding coefficient in the Fourier series representation of the periodic control input:

$$u_{[i,j]} = \sum_{k=1}^{\infty} \frac{1}{k} \left(\bar{u}_j A_i^{\sin,k} - \bar{u}_i A_j^{\sin,k} - \frac{1}{2} A_i^{\sin,k} A_j^{\cos,k} + \frac{1}{2} A_i^{\cos,k} A_j^{\sin,k} \right) \quad (14a)$$

$$[B_i, B_j] = \frac{\partial B_j}{\partial q} B_i - \frac{\partial B_i}{\partial q} B_j \quad (14b)$$

$$= \begin{bmatrix} \frac{\partial B_j^g}{\partial q} & \frac{\partial B_j^g}{\partial r} \\ \frac{\partial B_j^r}{\partial q} & \frac{\partial B_j^r}{\partial r} \end{bmatrix} \begin{bmatrix} B_i^g \\ B_i^r \end{bmatrix} - \begin{bmatrix} \frac{\partial B_i^g}{\partial q} & \frac{\partial B_i^g}{\partial r} \\ \frac{\partial B_i^r}{\partial q} & \frac{\partial B_i^r}{\partial r} \end{bmatrix} \begin{bmatrix} B_j^g \\ B_j^r \end{bmatrix} \quad (14c)$$

$$= \begin{bmatrix} [B_i^g, B_j^g] + \left(\frac{\partial B_j^g}{\partial r} B_i^r - \frac{\partial B_i^g}{\partial r} B_j^r \right) \\ \left(\frac{\partial B_j^r}{\partial r} B_i^r - \frac{\partial B_i^r}{\partial r} B_j^r \right) \end{bmatrix}, \quad (14d)$$

where all control vector fields B and their derivatives are evaluated at the nominal shape, B^g and B^r are the rows corresponding to the body and shape velocities, and B_i and B_j are the columns corresponding to the i - and j -th control inputs.

The accuracy of the approximation by truncation depends on three key factors: the frequency ω , the magnitude of the control vector field B in the control direction (which is influenced by the choice of coordinates describing the multi-link system's overall motion), and the amplitude of the control input. This dependency arises because all higher-order terms in the BCH series are products of exponential functions of the period T , high-order Lie brackets of the control vector field B , and multinomial terms of the mean and variation of the control input. A more detailed discussion on the approximation accuracy and the choice of coordinates to optimize this accuracy is provided in Appendix D. The aforementioned methodology can also be employed to determine the locomotion displacement resulting from periodic shape control, yielding results that align with prior research findings [45,46], as discussed in Appendix B.

The first-order Lie brackets constitute an additional set of vector fields, as shown in Fig. 6. These vector fields represent the passive state velocities that arise from alternating pairs of control inputs over a cycle. These additional vector fields complement the original control vector fields for states that cannot be directly and instantaneously controlled. By compiling all pairs of Lie brackets along with their corresponding amplitudes and appending them to the original control vector, we construct the augmented control vector field and augmented control input

$$B^{\text{aug}} = [B \quad [B_i, B_j]] \quad \text{for } i = 1, \dots, n-1, j = i+1, \dots, n \quad (15a)$$

$$u^{\text{aug}} = \begin{bmatrix} \bar{u} \\ \frac{1}{2\pi\omega} u_{[i,j]} \end{bmatrix} \quad \text{for } i = 1, \dots, n-1, j = i+1, \dots, n. \quad (15b)$$

Combining the first-order Lie bracket with the original control vector field, the augmented control vector field satisfies the

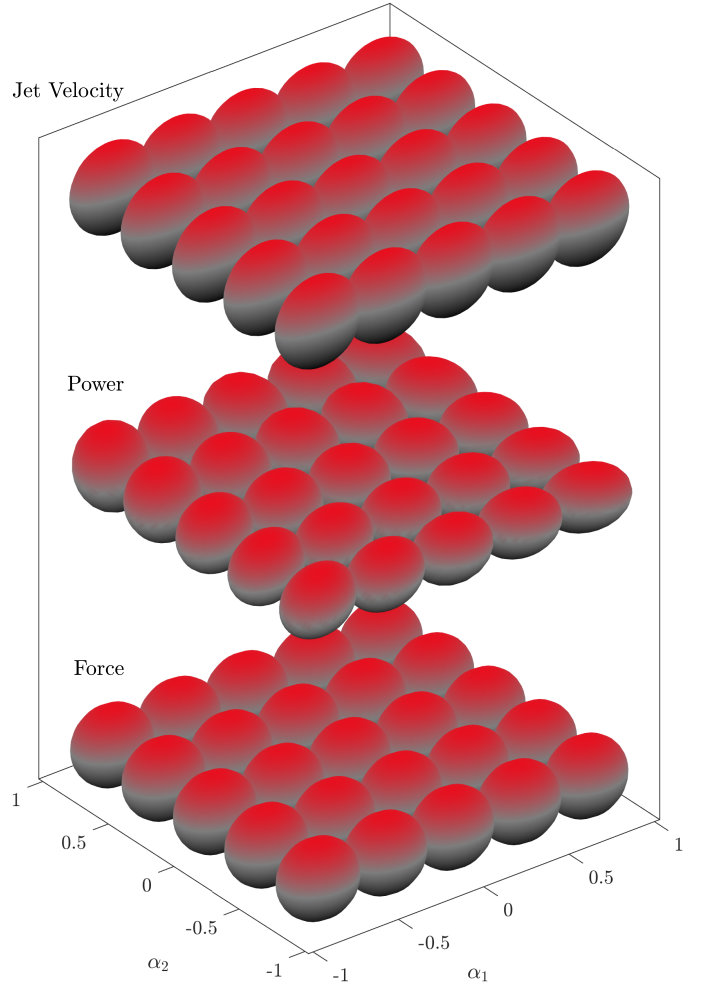


Fig. 7. The three control cost metrics for motion planning act as Riemann metrics on the control space. These metrics can be visualized via their Tissot indicatrices (the set of control vectors at each shape that produce a unit cost under the metric). The control space axes u_1 , u_2 , and u_3 are overlaid with the α_1 , α_2 , and height, respectively.

Lie algebra rank condition and ensures the small-time local controllability of the system.

B. Motion Planning and Feedback Control

Based on the averaging results, given the desired average velocity \dot{q}^{desired} , the control parameters in the form of a p -order Fourier series $\tilde{u} = [\bar{u} \quad A^{\sin,1} \quad A^{\cos,1} \quad \dots \quad A^{\sin,p} \quad A^{\cos,p}]^T$ around the nominal shape r^{nominal} can be determined by formulating a nonlinear programming problem

$$\min_{\tilde{u}} \|\tilde{u}\|_R^2 \quad (16a)$$

$$s.t. \quad \dot{q}^{\text{avg}} = \dot{q}^{\text{desired}}, \quad (16b)$$

where the control cost metric R can be selected to regularize (a) the average squared jet velocities, (b) the average dissipated

power, or (c) the average squared thrust force:

$$\|\tilde{u}\|_R^2 = \frac{1}{T} \int_0^T \|u(t)\|_{R_u}^2 dt \quad (17a)$$

$$R_u = \begin{cases} \text{diag} \left(\frac{1}{u_{1,\max}^2}, \frac{1}{u_{2,\max}^2}, \frac{1}{u_{3,\max}^2} \right) & \text{(Jet Velocity)} \\ J_u^\top D J_q B & \text{(Power)} \\ J_u^\top D^\top D J_u & \text{(Force)}, \end{cases} \quad (17b)$$

$$R = \text{diag} \left(R_u, \frac{1}{2}R_u, \frac{1}{2}R_u, \dots, \frac{1}{2}R_u, \frac{1}{2}R_u \right), \quad (17c)$$

where $u_{i,\max}$ is the maximum jet velocity (equivalent to the maximum velocity of the actuator in our LandSalp robot) for the i -th actuator, and R_u is a cometric tensor representing the cost of instantaneous control, which can be proposed in terms of jet velocity, power, or torque regularization.

Fig. 7 illustrates the Tissot indicatrices of three different cometric tensors within the shape space. The Tissot indicatrices represent the set of control vectors at each shape that produce a unit cost under the respective metric. It is evident that the jet velocity and force regularizations remain invariant with respect to shape, whereas power regularizations are shape-dependent. This invariance arises because both the jet velocity and force are inherent properties of the actuators and do not depend on the shape. Specifically, jet velocity regularization depends on the squared velocity limits of the three actuators, whereas force regularization is determined by the squared drag coefficients of these actuators along the jet direction. On the other hand, when the shape changes, certain modes of driving the wheels minimize the mechanical power that counterbalances within the system, becoming more efficient under the power regularizations, as reflected by the Tissot indicatrices.

Fig. 8 shows the forward gait corresponding to these three different cometrics in a straight configuration (zero joint angles). Given that the second actuator has a smaller maximum speed limit, jet velocity regularization is flatter along the u_2 direction, resulting in a slower gait cycle in u_2 . Conversely, to minimize the power and forces that are neutralized within the system, both power and force regularizations ensure that the three wheels operate at similar speeds, because they are nearly perpendicular to each other in a straight configuration. For the forward gait, the shape changes only slightly during the period (approximately 10 degrees in the first joint), as shown in Fig. 9. Consequently, the power regularization remains nearly constant and is similar to the force regularization. Compared to power regularization, force regularization causes the first and third wheels to drive slightly faster while slowing down the second wheel. This difference arises because force regularization incorporates the square of the drag coefficients when calculating the required cost, penalizing the second wheel slightly more. These regularized metric tensors are particularly useful when users aim to minimize specific costs based on the capabilities of the actuators.

The primary source of nonlinearity in this problem is the nonlinear constraint (16b), which poses significant challenges in optimization. Utilizing the analysis based on averaging the

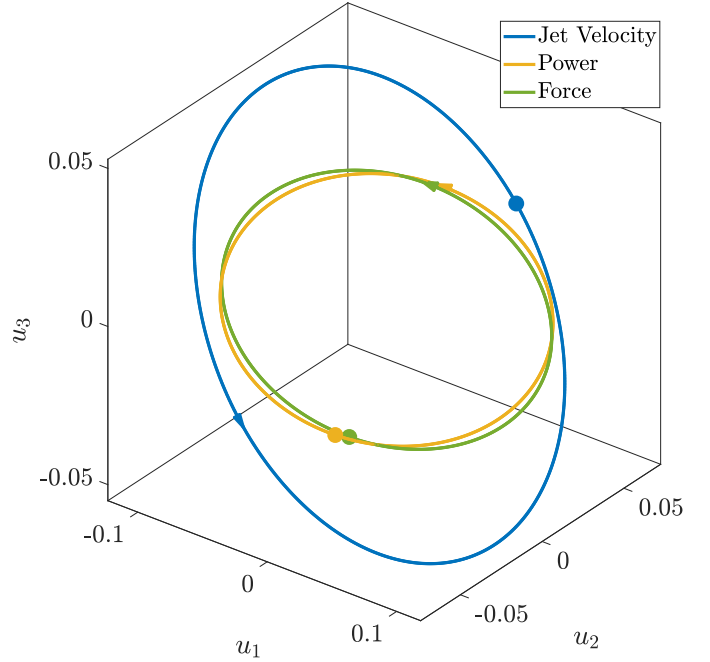


Fig. 8. Optimal forward gaits corresponding to three different cometrics at the $(0, 0)$ shape, where circle and triangle markers denote the initial phase and the gait direction, respectively. The velocity metric focuses on penalizing the speed of the second wheel, resulting in a contraction along that direction and an expansion in others. The power metric has a more uniform penalty across all three wheels, yielding a gait resembling a circle. Lastly, the torque metric imposes greater penalties on the first and second wheels compared to the power metric, consequently resulting in increased speeds for the third wheel.

ory as discussed in (13e), we can approximate this constraint by the averaged results. This approach allows us to derive analytical gradients and Hessians from the analysis, achieving a more tractable optimization process.

$$\|\tilde{u}\|_R^2 \quad \tilde{u}^\top R \tilde{u} \quad (18a)$$

$$s.t. \quad B^{\text{aug}} u^{\text{aug}}(\tilde{u}) = \dot{q}^{\text{desired}}. \quad (18b)$$

In contrast to shape-controlled systems, which typically employ the optimal gait derived from the average system directly [22,23], force-controlled systems require that the optimal gait, serving as the feedforward component in the closed-loop control, must be a strict equilibrium to ensure stability. Otherwise, feedback control cannot stabilize the system. Therefore, after determining the optimal gait for the averaged system, it is necessary to refine this gait within the full system using finite-difference methods.

Because the optimal gait is computed around a nominal shape, any perturbation or model mismatch may cause deviation from this nominal shape, thus invalidating the optimal gait. Therefore, we incorporate feedback control into the system. Following the methodology proposed in [47,48], we linearize the averaged system at the nominal shape r^{nominal} and the optimal gait \tilde{u}

$$\Delta \dot{q} \approx \frac{\partial B^{\text{aug}}(r^{\text{nominal}}) u^{\text{aug}}(\tilde{u})}{\partial q} \Delta q + \frac{\partial B^{\text{aug}}(r^{\text{nominal}}) u^{\text{aug}}(\tilde{u})}{\partial \tilde{u}} \Delta \tilde{u}, \quad (19)$$

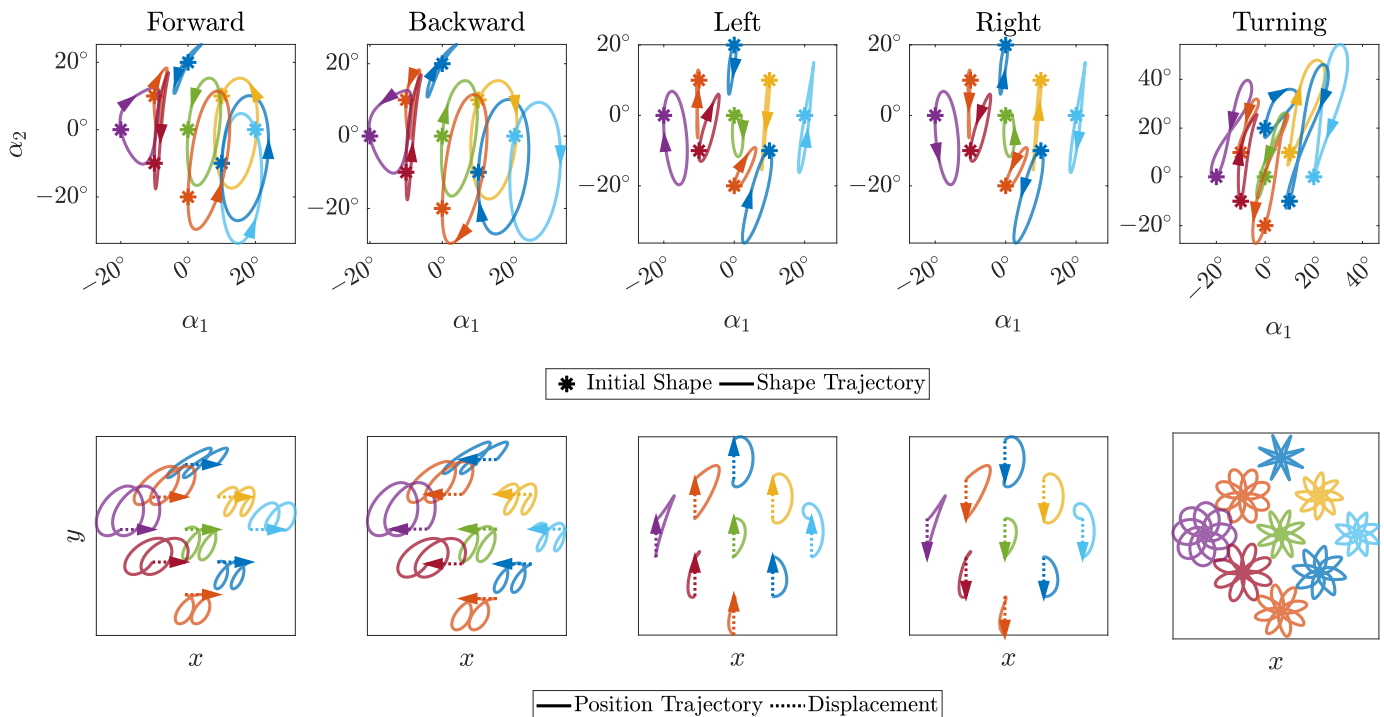


Fig. 9. LandSalp simulation results for forward, backward, left, right, and turning motions. The first row shows the shape trajectory and nominal shape of the robot, with arrows indicating the direction of motion. The second row illustrates the position trajectory and net displacement of each nominal shape over 2, 1, and 8 gait cycles corresponding to forward-backward, left-right, and turning motions, respectively.

and then discretize¹⁵ by the gait period T to design a discrete linear quadratic regulator with the state feedback gain K for updating the control \tilde{u} at each gait cycle to correct the error in $q = [g^\top \ r^\top]^\top$

$$\tilde{u}(t) = \tilde{u}_0 - K (q^{\text{desired}}(t_k) - q(t_k))$$

for $t \in [t_k, t_{k+1})$, where $t_k = kT, k \in \mathbb{Z}_{\geq 0}$, (20)

where \tilde{u}_0 is the feedforward optimal gait. As discussed in [48], because the averaged system satisfies the Lie algebra rank condition, the full system can be stabilized by stabilizing the averaged system.

Note that when the shape velocity is set to zero, this formulation guarantees that the initial and terminal shapes remain unchanged. In our implementation, we define the initial shape as the nominal shape r^{nominal} , which implies that the shape trajectory will pass through this nominal shape. However, this choice may not always be advantageous. For instance, if the nominal shape is close to the joint limits, the resulting trajectory may be more likely to violate these constraints. Moreover, the average shape over the gait cycle might not align with the nominal shape, thereby degrading the approximation accuracy of the averaging theory. In practical applications, the proposed feedback controller mitigates this issue and compensates for model mismatches and external disturbances. Readers interested in a more theoretical treatment of this problem are encouraged to read Appendix C, which provides additional constraints for simultaneously solving the initial shape and optimal gait to ensure that the shape trajectory

over the gait cycle averages at the desired shape.

VI. EXPERIMENT EVALUATION

To assess the efficacy of the proposed modeling and control methodology, we conduct experiments in both simulation and hardware. In simulation, we employ the data-driven geometric model learned from experimental data to demonstrate the capability of our approach to finding optimal gaits for different nominal shapes and desired velocities. On the LandSalp hardware platform, we execute these optimal gaits and corresponding feedback controllers to validate their locomotion performance as well as measure displacement errors and evaluate the precision of the model predictions.

A. Simulation Evaluation

We first used the proposed motion planning method to generate optimal gaits for various locomotion directions and nominal shapes to test its effectiveness. We explored five different locomotion modes: forward, backward, left, right, and clockwise turning. The gait period was set at 1/6 Hz. The velocities for forward and backward locomotion were 3 cm/cycle, while for left and right motions, the velocities were 6 cm/cycle. The turning speed was 45 deg/cycle. These velocity parameters were designed to ensure that the maximum drive speed remained within the actuator limitations and maintained traction without slipping on a flat surface. All gaits were optimized to minimize the mechanical power of the actuators.

¹⁵In our implementation, we apply an exponential mapping to the logarithmic average velocity to obtain the discrete system dynamics.

In the evaluation, all gaits are characterized using a first-order Fourier series. The simulation model used physical coefficients derived from experimental data.

Fig. 9 illustrates the shape and position trajectories for locomotion in various directions and for different nominal shapes. In these experiments, forward and backward motions are executed for 2 cycles, left and right motions for 1 cycle, and turning motions for 8 cycles to enhance visualization clarity. The results demonstrate that the proposed motion planning algorithm effectively finds the open-loop optimal gaits that maintain periodic equilibrium and drive the robot in the desired direction.

Notably, turning or lateral movements exhibit greater efficiency compared to forward and backward movements. This increased efficiency can be attributed to the alternating lateral deflection of the wheels along the link's long axis, which leads to significant internal cancellation of driving forces during longitudinal motion, but much less cancellation during lateral and turning locomotion. The optimal gaits for locomotion in opposite directions are symmetrical and phase-opposite. However, the open-loop stability of gaits in opposite directions varies, leading to significant differences in feedback control, which will be further discussed in the hardware evaluation section.

The range of shape motion for some gaits is significantly larger than for others, depending on the nominal shape, which may increase the likelihood of failure and approaching joint limits when implemented on hardware. Turning motions, especially, cause substantial joint movements, particularly when the nominal shape is distant from the straight configuration. Such large deviations from the nominal shape may invalidate the averaging around the nominal shape. To mitigate this, a potential solution is to explicitly enforce joint limits and constrain the average of the shape trajectories to match the nominal shape during optimization, thereby ensuring feasibility (see Appendix C). Overall, the nominal shape at the straight configuration has the smallest shape motion range and remains distant from the joint limits.

B. Hardware Evaluation

We conducted the hardware evaluation of the proposed methods by commanding the LandSalp to move in different directions while maintaining a nominal shape of zero joint angles. The experimental setup is shown in Fig. 10. The LandSalp robot ran on a flat platform, utilizing OptiTrack motion capture for state estimation, feedback control, and ground truth data collection. The robot was powered through tension-free cables and controlled via an external laptop connected through Ethernet. The laptop ran ROS Noetic, receiving motion capture data at a frequency of 240 Hz and transmitting control commands to each actuator at a frequency of 200 Hz.

Given that the bottleneck of the system is the maximum speed of the actuators, we have chosen to regularize the jet velocity within the motion planning and control processes. Furthermore, we implement the discrete feedback as proposed in (20) within each cycle. In our implementation, all gaits are represented using a first-order Fourier series.



Fig. 10. LandSalp experiment setup. The robot runs on a platform integrated with the OptiTrack motion capture system. Motion capture data is processed by a desktop computer and subsequently transmitted via the Robot Operating System (ROS) to a laptop that executes the control algorithm. The robot is connected by two cables, one for power supply and the other for command signals.

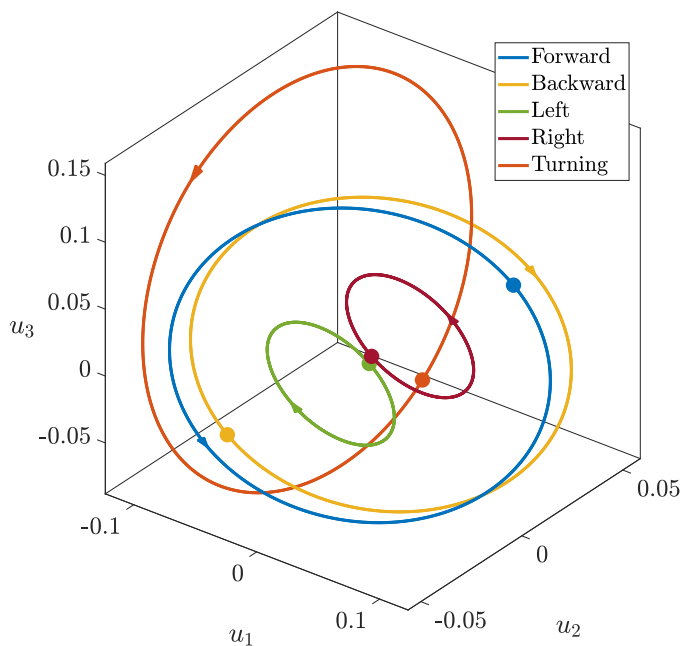


Fig. 11. Optimal gaits for forward, backward, left, right, and turning motions under the velocity cost. The circle and triangle markers denote the initial phase and the gait direction, respectively. A notable observation is that opposite motions have mirrored gaits relative to the zero joint angles, despite variations in linearization and feedback control.

Fig. 11 shows the optimal gaits tested in the hardware evaluation. Similar to the simulation evaluation, the robot was commanded to move forward, backward, left, right, and clockwise at its nominal shape with zero joint angles. The forward and backward motions were executed at a speed of 3 cm/cycle for 15 cycles, the left and right movements were conducted at a speed of 6 cm/cycle for 8 cycles, and the turning motion was performed at 45 deg/cycle for 8 cycles. The forward-backward and turning gaits are performed with

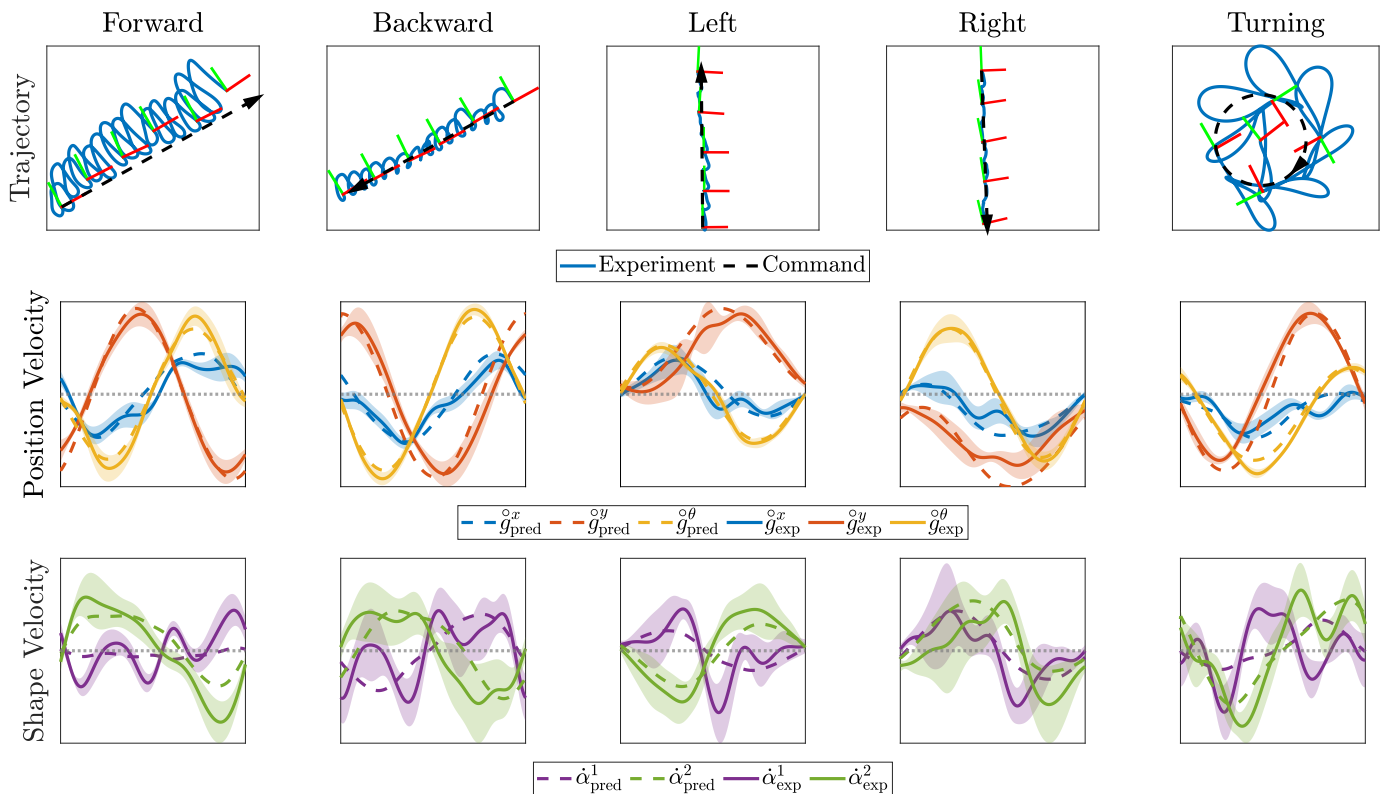


Fig. 12. Experimental results of LandSalp’s forward, backward, left, right, and turning motions. The first row shows the robot’s commands and the experimental trajectories and orientations. The second row illustrates the average model-predicted and experimental position velocities, as well as the corresponding standard deviations, over a gait cycle. The third row displays the average model-predicted and experimental shape velocities, along with their standard deviations, over a gait cycle.

actuator speeds close to maximum, while the lateral gaits are relatively more efficient.

Consistent with theoretical predictions from simulations, the optimal gaits for two opposite directions were symmetrical within the control space and had reverse phases. However, their stability and feedback control varied significantly due to the asymmetry of the control vector field, which is also evident from the robot’s asymmetric geometry. This asymmetry is the primary reason for excluding counterclockwise motion in the experiments with the used robot hardware configuration. Intuitively, it is evident from the robot’s geometry that instability arises in the counterclockwise direction because the required inward driving force of the side wheels induces joint buckling and link collision. Conversely, clockwise motion is more easily stabilized as the outward movement of the side wheels generates the required torque while also maintaining the robot’s shape by pulling it apart from both sides.

The first row of Fig. 12 illustrates the locomotion trajectories for the tested motions. The frame and trajectory represent the system body frame, determined by the center of mass and the average orientation of the three links. The robot effectively tracks commands in all directions, although with greater accuracy in backward compared to forward motions, and leftward compared to rightward movements. This discrepancy can be attributed to the asymmetric geometry of the robot and the consequent asymmetric control vector field, as discussed previously. Consequently, the feedback controller

requires more effort to stabilize motion in one direction compared to its opposite. Feedback that actively compensates for locomotion errors due to unmodeled effects or disturbances is crucial. Specifically, in forward motion, feedback control mitigates lateral drift, and during rightward motion, it minimizes orientation errors. In summary, the tracking error for all directions stays small enough to be compensated for by a higher-layer tracking controller.

The second and third rows of Fig. 12 show the average values of both experimental and model-predicted position and shape velocities across all cycles of the experiment. The shaded regions represent the standard deviations of these statistical values. It is evident that the shape velocity varies more than the position velocity across different gait cycles. This increased variability may be attributed to the passive nature of the joints, which are more susceptible to perturbations than the overall system position. Additionally, the position velocity in lateral motion shows slightly more variation than in other directions, possibly due to the higher command velocity for lateral motion. More importantly, the model’s predictions effectively capture the primary trends in both position and shape velocities, thereby ensuring good control performance. The model’s predictions for position velocity are more accurate than those for shape velocity, where the experimental data indicate some second-order effects resembling spring behavior caused by the harness on the robot, which exceeds the scope of our first-order model. Nevertheless, the model successfully



Fig. 13. Snapshots of the forward, backward, left, right, and turning motions of the LandSalp experiment. The first four rows show the robot’s positions at approximately the quarter intervals of the entire motion cycle, as well as the configurations corresponding to the quarter intervals of the gait cycle. The last row presents the robot’s configurations at the quarter points of the gait cycle during a single gait of clockwise turning. The white arrows indicate the desired direction of velocity.

captures the first-order trends in joint velocities. Extending our model and methodology to incorporate second-order effects is a key element of our envisioned future work.

Each row of Fig. 13 illustrates a series of snapshots depicting the LandSalp locomoting in various directions. From the snapshots, we can again find the symmetry between the two pairs of opposite locomotion directions: forward-to-backward and left-to-right. During forward or backward movement, LandSalp first bends its head and tail to align the omniwheels’ rollers to minimize drag, then drives the robot forward using the central wheel, and finally returns the head and tail back. For lateral motions, the LandSalp first rotates itself by driving the two side wheels. Once the required displacement is achieved, it halts one side and propels the robot using the central and outer wheels, thereby correcting the tail’s rotation while maintaining the lateral displacement. When performing turning locomotion, the LandSalp generates a rotational moment by driving the two side links in opposite directions and then uses the central and head wheels to correct positional errors and shape drift. Notably, during turning, the

tail link is pulled by the cable upon reaching the far end, resulting in a significant shape error. In the subsequent gait cycle, feedback control actively adjusts the gait to fix this error.¹⁶

Overall, the optimal gaits successfully achieve accurate omnidirectional locomotion in a reasonable manner within the constraints of actuator capabilities during hardware evaluations. These results demonstrate the effectiveness of the proposed geometric model, data-driven geometric model identification, and geometric motion planning and control methodologies. Furthermore, the locomotion behavior of LandSalp offers valuable insights into the underwater locomotion of salps and provides a path towards the development of more capable salp-inspired underwater robots.

VII. CONCLUSION AND FUTURE WORKS

In this paper, we introduce a comprehensive geometric mechanics framework for the study of underwater locomo-

¹⁶Readers interested in further details can refer to the locomotion video provided in the supplementary material.

tion inspired by salps, including the modeling of underwater locomotion based on viscous drag, the design of the LandSalp robot, data-driven geometric model identification, and geometric motion planning and control.

The geometric modeling for underwater locomotion for salps based on viscous drag enables the encoding of complex underwater locomotion via a set of local metrics. This approach is consistent with the unified geometric modeling paradigm established in prior research. More importantly, this model allows us to reproduce essentially the same physics of salp swimming on the LandSalp robot with series-elastic actuators, while avoiding the overhead of underwater operation. This approach creates a clear path for scaling our approach to more complex underwater robotic systems.

A key feature of the geometric framework is its support for efficient data-driven model identification, which enables the identification of model coefficients from only about 3 minutes of experimental data using a semidefinite programming approach. This efficiency highlights both the compactness and effectiveness of the geometric model, underscoring its potential for practical applications. Moreover, the framework’s generality in identifying Riemannian metrics that encode system dynamics suggests its applicability to a wide range of bio-inspired robotic systems.

Finally, we extend the geometric motion planning and control framework based on averaging theory to the force-controlled multi-jet system where stability considerations are significant. Our approach can determine the optimal gait and feedback controller for any given desired velocity and nominal shape based on three different power cost metrics. Both simulation and hardware evaluations indicate that the optimal gait and feedback controller can achieve precise omnidirectional locomotion while ensuring stability. The promising evaluation results demonstrate the effectiveness of the proposed framework and provide a foundation for future applications to more bio-inspired robots and more complex locomotion scenarios.

One immediate direction for future work is adapting our methods to underwater robots propelled by thrusters. This extension would allow us to transfer our insights from the LandSalp to an aquatic environment and tackle the challenges and opportunities of field robotic deployment. Moreover, water-based platforms offer an ideal testbed for evaluating salp-inspired soft jet propulsion units [11].

Beyond the design of the robotic system and jet mechanism, the integration of onboard sensing and state estimation is critical for field deployment. Specifically, inertial measurement units and joint encoders can be used to construct a state estimator based on the proposed locomotion model [40], which is essential for data collection and feedback control. Potential research directions in this domain also include optimizing sensor placement [49–51] and developing motion planning strategies to enhance information gathering efficacy [52–54].

The onboard state estimation enables the proposed data-driven modeling with only proprioceptive data. This demonstrates the versatility of the proposed approach and suggests future research opportunities that incorporate our methods with onboard sensing to achieve online data-driven model identification [55,56] and iterative learning control [30], thereby

enabling the identification of changes in the swimming environment or the docking and undocking of salp units from the salp robot.

It is important to note that our data-driven modeling approach is not limited to drag-dominated kinematic model. The proposed idea of utilizing the geometric structure to efficiently extract the Riemannian metric that determines the system dynamics from experimental data can be generalized to more general dynamic data-driven models, including inertia with fluid-added mass as well as the stiffness of the salp body [36]. Additional unmodeled effects, potentially arising from vortices and other complex fluid dynamics, can be incorporated by combining the proposed method with the application of Gaussian process [57] or Koopman operator theory [58].

As shown in the experimental results, some second-order dynamic effects emerge in the system. This behavior may be more pronounced when we apply the same approach to an underwater robot. To address this, we can apply the methods outlined in Section V to the dynamic model to find optimal oscillation control based on controllability analysis, similar to [20]. To mitigate drift effects in the dynamics, the method discussed in [59] can be used to refine the gait under conditions of non-zero net momentum.

Finally, another potential avenue for future research involves extending to higher-level path planning that integrates the low-level control proposed in this study. When the command is beyond local velocity and involves waypoints or trajectories, determining the optimal path to track these directives in complex environments with obstacles becomes a challenging problem. This issue can be approached either as a trajectory planning problem that incorporates full dynamics [60,61], or as a hierarchical framework, where we first generate motion primitives or a gait library [62] and subsequently address the path planning problem [63]. In addition, considering the reconfigurable properties of salps, there are also more potential future works in the decision-making field, such as constructing motion plans for salp-inspired robots with reconfiguration capabilities [64].

APPENDIX A GROUP ACTION AND DIFFERENTIATION

In this paper, we take several derivatives with respect to right group actions, producing left-invariant representations of velocity and force. The “open circle” oversets represent tangent vectors, such as velocity, and the undersets are for covectors such as force or momentum. Following convention, velocity is represented as the time derivative of the configuration (with the open circle acting in the role of the dot), and momentum and force are given their own symbols (rather than marking them as derivatives of energy terms).

For example, the full reading of the notation of the body velocity $\overset{\circ}{g}$ is “the velocity constructed by taking the derivative of position with respect to right group actions”

$$\overset{\circ}{g} = g^{-1}\dot{g}, \quad (21)$$

and the full reading of the notation of body force f is “the force constructed by taking the derivative of dissipated energy with respect to right (body) velocities”

$$E = \frac{1}{2} \langle f; \mathring{g} \rangle. \quad (22)$$

Similarly, given a time series of group elements, we can apply Lie-group time differentiation to obtain a discrete approximation of the body velocity in the corresponding Lie algebra, which better aligns with the underlying geometric structure:

$$\mathring{g}(t) = \frac{1}{\Delta t} \log (g(t)^{-1} g(t + \Delta t)). \quad (23)$$

Unlike finite differencing in Euclidean space, which takes the underlying trajectory as linearly interpolating between evaluation points, Lie-group differentiation uses an arc interpolation which naturally captures the intrinsic coupling between translation and rotation for systems whose dynamics are expressed in their body frames.

APPENDIX B

USE AVERAGING THEORY FOR SHAPE-CONTROLLED SYSTEM

In this paper, we consider systems where forces serve as the controlled input. It is noteworthy that the same analytical framework can be extended to systems with shape control. The application of averaging theory in the locomotion analysis of these systems offers significant insights into geometric motion planning.

Suppose that we can directly control shape velocity to achieve locomotion, i.e. $\mathring{g} = B(r)\dot{r}$, which is a common setting in many previous studies on geometric motion planning [22,23,33,45]. The averaging process outlined in (13e) is still applicable and becomes

$$\mathring{g}^{\text{avg}T} = \log g(T) \quad (24a)$$

$$= \log \left(\prod_0^T \exp(B\dot{r}(t)dt) \right) \quad (24b)$$

$$= \int_0^T B\dot{r}(t)dt + \int_0^T \frac{1}{2} \left[B\dot{r}(t), \left(\int_t^T B\dot{r}(\tau)d\tau \right) \right] dt + \dots \quad (24c)$$

$$\approx \int_0^T B\dot{r}(t)dt + \int_0^T \frac{1}{2} \left[B\dot{r}(t), \left(\int_t^T B\dot{r}(\tau)d\tau \right) \right] dt \quad (24d)$$

$$= \oint \left(\mathbf{d}B + \sum_{i,j>i} [B_i, B_j] \right), \quad (24e)$$

where the generalized Stokes’ theorem is applied to the line integral, and the one-half factor is canceled by the antisymmetric property of the Lie brackets, resulting in integrals over 2-surfaces in the shape space. It is important to highlight that there is no necessity to assume a constant control vector field

at the nominal shape in this case, because we are directly working within the shape space and integrating the control vector field therein. This result aligns with the total Lie bracket described in the previous geometric mechanics literature [45], and can be extended for higher-order approximations as discussed in [46].

APPENDIX C

GAIT OPTIMIZATION CONSIDERING AVERAGE SHAPE AND JOINT LIMITS

As demonstrated by the shape trajectories observed in the simulation evaluations, for certain nominal shapes far from the zero joint angles, the shape trajectory within a single gait cycle can exhibit substantial deviations from the nominal shape and approach the joint limits. Given that the linearization is performed around the nominal shape, such large deviations can invalidate the feedback control. In addition, considering the joint limitations of the robot, large joint motions can potentially result in collisions between links.

To address this issue, a possible solution involves incorporating additional decision variables and constraints into the motion planning optimization to ensure that the nominal shape is the average of the shape trajectories throughout the gait cycle. Specifically, we can introduce a new variable, r_0 , representing the initial shape of the gait cycle, rather than assuming that the gait starts and ends with the nominal shape. Additionally, it is necessary to impose a constraint such that the mean of the shape trajectories within the gait cycle is the nominal shape. The new optimization problem can be formulated as follows:

$$\min_{\tilde{u}, r_0} \tilde{u}^T R \tilde{u} \quad (25a)$$

$$s.t. \quad \frac{1}{T} \log g(T) - \dot{q}^{\text{desired}} = 0 \quad (25b)$$

$$\frac{1}{T} \int_0^T r(t)dt = r^{\text{nominal}} \quad (25c)$$

$$r(t) \in \mathcal{R} \quad \forall t, \quad (25d)$$

where \mathcal{R} is the joint limit.

The new optimization formula better guarantees that the optimal gait converges to the nominal shape on average, thereby ensuring linearization performance while minimizing the risk of the range of motion exceeding joint limits. However, this modification increases the complexity of the optimization. In particular, the solution for the constrained optimization can differ significantly from that obtained using an approximate optimization based on the averaged system, complicating any preliminary rough search for the optimal gait. Given the challenge of analytically obtaining the gradient in the full optimization and the inefficiency of finite-difference methods, this optimization may not be feasible. Additionally, this formula imposes higher demands on the feedback control, because the shape trajectory is constrained to average to the nominal shape rather than passing directly through it. One possible feedback strategy is to integrate the shape online over the gait cycle and use the difference between the integrated average and the nominal shape as the error signal in the

feedback loop. In practice, when operating near the zero joint angles, the shape trajectory span is relatively small, so it is not necessary to use this formula. In future work, this new formula can be used for more demanding tasks.

APPENDIX D

AVERAGING ACCURACY AND COORDINATE OPTIMIZATION

As previously noted, the accuracy of the average approximation in (13e) depends on the proportion of the truncated higher-order terms in the BCH series. To enable the use of gaits with low frequency and large control input, it is essential to maintain approximation accuracy. Because all higher-order terms involve higher-order Lie brackets of the control vector field B , to improve accuracy, we can identify the optimal coordinates with transformation $g_{\text{coord}}(r)$ relative to the original coordinates. This transformation aims to minimize the magnitude of the control vector field over a region of interest Ω in the shape space, thereby minimizing the proportion of the truncated higher-order terms

$$B_{\text{new}} = \begin{bmatrix} Ad_{g_{\text{coord}}}^{-1} & 0 \\ 0 & \text{Id} \end{bmatrix} B + \begin{bmatrix} g_{\text{coord}} \\ 0 \end{bmatrix} \quad (26a)$$

$$g_{\text{coord}}^* = \underset{g_{\text{coord}}}{\operatorname{argmin}} \int \dots \int_{r \in \Omega} \|B_{\text{new}}(r)\|_F^2 d\Omega. \quad (26b)$$

The above minimization problem is a partial differential equation. Previous works have introduced two different methods for determining the optimal coordinates: one involves discretizing the shape space into a grid [33], and the other entails sampling along the gait within the shape space [32]. Solutions to the minimization tend to place the system body frame near its center of mass and the mean orientation of the links; in many cases sufficient accuracy can be achieved by using such an averaged frame directly instead of performing the optimization.

It is worth noting that changing the coordinates does not affect the magnitude of the control vector field in the direction of the shape, as shown in (26a), which demonstrates a key distinction between force control systems and shape control systems. Therefore, the stability of a control scheme based on averaging theory will depend on the variation of the control vector field around the nominal shape. One possible direction is to consider the variations in the control vector field during motion planning, rather than assuming the shape remains constant at its nominal value.

REFERENCES

- [1] Q. Bone and E. R. Trueman, "Jet propulsion in salps (Tunicata: Thaliacea)," *Journal of Zoology*, vol. 201, no. 4, pp. 481–506, Dec. 1983.
- [2] P. F. Linden and J. S. Turner, "'Optimal' vortex rings and aquatic propulsion mechanisms," *Proceedings of the Royal Society of London. Series B: Biological Sciences*, vol. 271, no. 1539, pp. 647–653, Mar. 2004.
- [3] K. R. Sutherland and L. P. Madin, "Comparative jet wake structure and swimming performance of salps," *Journal of Experimental Biology*, vol. 213, no. 17, pp. 2967–2975, Sep. 2010.
- [4] K. R. Sutherland and D. Weihs, "Hydrodynamic advantages of swimming by salp chains," *Journal of The Royal Society Interface*, vol. 14, no. 133, p. 20170298, Aug. 2017.
- [5] A. Damian-Serrano, K. A. Walton, A. Bishop-Perdue, S. Bagoeye, K. T. Du Clos, B. J. Gemmill, S. P. Colin, J. H. Costello, and K. R. Sutherland, "Colonial Architecture Modulates the Speed and Efficiency of Multi-Jet Swimming in Salp Colonies," Apr. 2024.
- [6] A. Villanueva, C. Smith, and S. Priya, "A biomimetic robotic jellyfish (Robojelly) actuated by shape memory alloy composite actuators," *Bioinspiration & Biomimetics*, vol. 6, no. 3, p. 036004, Sep. 2011.
- [7] K. Marut, C. Stewart, T. Michael, A. Villanueva, and S. Priya, "A jellyfish-inspired jet propulsion robot actuated by an iris mechanism," *Smart Materials and Structures*, vol. 22, no. 9, p. 094021, Sep. 2013.
- [8] F. Renda, F. G. Serchi, F. Boyer, and C. Laschi, "Structural Dynamics of a Pulsed-Jet Propulsion System for Underwater Soft Robots," *International Journal of Advanced Robotic Systems*, vol. 12, no. 6, p. 68, Jun. 2015.
- [9] V. L. Gatto, J. M. Rossiter, and H. Hauser, "Robotic jellyfish actuated by soft finray effect structured tentacles," in *2020 3rd IEEE International Conference on Soft Robotics (RoboSoft)*. New Haven, CT, USA: IEEE, May 2020, pp. 144–149.
- [10] Z. Yang, D. Chen, D. J. Levine, and C. Sung, "Origami-inspired robot that swims via jet propulsion," *IEEE Robotics and Automation Letters*, vol. 6, no. 4, pp. 7145–7152, Oct. 2021.
- [11] A. Jones and J. R. Davidson, "Underwater salp-inspired soft structure contraction with twisted coiled actuators," in *2024 IEEE 7th International Conference on Soft Robotics (RoboSoft)*. San Diego, CA, USA: IEEE, Apr. 2024, pp. 504–510.
- [12] X. Dong, H. Chen, Z. Zhou, C. Ouyang, L. Hu, F. Zhang, B. Chen, and Z. Gan, "Salpot: A Jet Propulsion Swimmer With Scissor Structure and Bilateral Apertures," *IEEE Robotics and Automation Letters*, vol. 9, no. 8, pp. 7102–7109, Aug. 2024.
- [13] I. Aljarah, M. Mafarja, A. A. Heidari, H. Faris, Y. Zhang, and S. Mirjalili, "Asynchronous accelerating multi-leader salp chains for feature selection," *Applied Soft Computing*, vol. 71, pp. 964–979, Oct. 2018.
- [14] A. A. Ateya, A. Muthanna, A. Vybornova, A. D. Algarni, A. Abuarqoub, Y. Koucheryavy, and A. Koucheryavy, "Chaotic salp swarm algorithm for SDN multi-controller networks," *Engineering Science and Technology, an International Journal*, vol. 22, no. 4, pp. 1001–1012, Aug. 2019.
- [15] N. Rokbani, S. Mirjalili, M. Slim, and A. M. Alimi, "A beta salp swarm algorithm meta-heuristic for inverse kinematics and optimization," *Applied Intelligence*, vol. 52, no. 9, pp. 10493–10518, Jul. 2022.
- [16] H. Ding, X. Cao, Z. Wang, G. Dhiman, P. Hou, J. Wang, A. Li, and X. Hu, "Velocity clamping-assisted adaptive salp swarm algorithm: Balance analysis and case studies," *Mathematical Biosciences and Engineering*, vol. 19, no. 8, pp. 7756–7804, 2022.
- [17] A. E. Romeh and S. Mirjalili, "Multi-Robot Exploration of Unknown Space Using Combined Meta-Heuristic Salp Swarm Algorithm and Deterministic Coordinated Multi-Robot Exploration," *Sensors*, vol. 23, no. 4, p. 2156, Feb. 2023.
- [18] J. P. Ostrowski, "The mechanics and control of undulatory robotic locomotion," Ph.D. dissertation, California Institute of Technology, 1996.
- [19] K. McIsaac and J. Ostrowski, "Motion planning for anguilliform locomotion," *IEEE Transactions on Robotics and Automation*, vol. 19, no. 4, pp. 637–652, Aug. 2003.
- [20] K. A. Morgansen, B. I. Triplett, and D. J. Klein, "Geometric methods for modeling and control of free-swimming fin-actuated underwater vehicles," *IEEE Transactions on Robotics*, vol. 23, no. 6, pp. 1184–1199, Dec. 2007.
- [21] R. L. Hatton, Y. Ding, H. Choset, and D. I. Goldman, "Geometric Visualization of Self-Propulsion in a Complex Medium," *Physical Review Letters*, vol. 110, no. 7, p. 078101, Feb. 2013.
- [22] S. Ramasamy and R. L. Hatton, "The geometry of optimal gaits for drag-dominated kinematic systems," *IEEE Transactions on Robotics*, vol. 35, no. 4, pp. 1014–1033, Aug. 2019.
- [23] R. L. Hatton, Z. Brock, S. Chen, H. Choset, H. Faraji, R. Fu, N. Justus, and S. Ramasamy, "The geometry of optimal gaits for inertia-dominated kinematic systems," *IEEE Transactions on Robotics*, vol. 38, no. 5, pp. 3279–3299, Oct. 2022.
- [24] O. Xie, Q. Zhu, L. Shen, and K. Ren, "Kinematic study on a self-propelled bionic underwater robot with undulation and jet propulsion modes," *Robotica*, vol. 36, no. 11, pp. 1613–1626, Nov. 2018.
- [25] Y. Li, L. Liu, Y. Wang, and C. Ren, "Hydrodynamic analysis and motion control of the Coanda-effect jet thruster for underwater robots," *Ocean Engineering*, vol. 266, p. 113096, Dec. 2022.
- [26] Y. Takagi, M. Ishikawa, and K. Osuka, "A kinematic-dual snake robot: Undulatory mobile robot driven by controllable side-thrust links," *Mechatronics*, vol. 90, p. 102944, Apr. 2023.
- [27] CallieSanDiego, "Common salp [photograph]," <https://www.inaturalist.org/observations/232074887>, 2024, observed on July 26, 2024 at

- HMCS Yukon, San Diego, CA. Licensed under CC BY-NC 4.0 (<https://creativecommons.org/licenses/by-nc/4.0/>). Accessed on March 07, 2025.
- [28] F. Rozaidi, E. Waters, O. Dawes, J. Yang, J. R. Davidson, and R. L. Hatton, "HISSbot: Sidewinding with a soft snake robot," in *2023 IEEE International Conference on Soft Robotics (RoboSoft)*, Apr. 2023, pp. 1–7.
- [29] C. Sparks, N. Justus, R. Hatton, and N. Gravish, "Amoeba-inspired swimming through isoperimetric modulation of body shape," in *2022 IEEE/RSJ International Conference on Intelligent Robots and Systems (IROS)*, Oct. 2022, pp. 2685–2692.
- [30] B. Bittner, R. L. Hatton, and S. Revzen, "Geometrically optimal gaits: A data-driven approach," *Nonlinear Dynamics*, vol. 94, no. 3, pp. 1933–1948, Nov. 2018.
- [31] S. Even, P. S. Martinez, C. Keogh, O. Gross, Y. Ozkan-Aydin, and P. Schröder, "A variational approach to geometric mechanics for undulating robotic locomotion," Sep. 2024. [Online]. Available: <https://arxiv.org/abs/2409.10827>
- [32] Y. Yang, C. Bass, and R. L. Hatton, "Towards geometric motion planning for high-dimensional systems: Gait-based coordinate optimization and local metrics," in *2024 IEEE International Conference on Robotics and Automation (ICRA)*. Yokohama, Japan: IEEE, May 2024, pp. 18 494–18 500.
- [33] R. L. Hatton, L. J. Burton, A. E. Hosoi, and H. Choset, "Geometric maneuverability with applications to low reynolds number swimming," in *2011 IEEE/RSJ International Conference on Intelligent Robots and Systems*. San Francisco, CA: IEEE, Sep. 2011, pp. 3893–3898.
- [34] G. Walsh and S. Sastry, "On reorienting linked rigid bodies using internal motions," *IEEE Transactions on Robotics and Automation*, vol. 11, no. 1, pp. 139–146, Feb. 1995.
- [35] N. Hecht, Y. Yang, F. Rozaidi, and R. L. Hatton, "Design of a planar, salp-like robot," in *ICRA 2024 Workshop on Unconventional Robots: Universal Lessons for Designing Unique Systems*, May 2024.
- [36] N. T. Justus, "The geometry of passive and constrained locomotion," Ph.D. dissertation, Oregon State University / Oregon State University, Jun. 2024.
- [37] A. Damian-Serrano and K. R. Sutherland, "A Developmental Ontology for the Colonial Architecture of Salps," *The Biological Bulletin*, vol. 245, no. 1, pp. 9–18, Aug. 2023.
- [38] A. Bloch, *Nonholonomic Mechanics and Control*. Springer New York, 2015.
- [39] R. L. Hatton and H. Choset, "Approximating displacement with the body velocity integral," in *Robotics: Science and Systems*, Jun. 2009.
- [40] D. Rollinson, A. Buchan, and H. Choset, "State estimation for snake robots," in *2011 IEEE/RSJ International Conference on Intelligent Robots and Systems*. San Francisco, CA: IEEE, Sep. 2011, pp. 1075–1080.
- [41] J. R. Magnus and H. Neudecker, *Matrix Differential Calculus with Applications in Statistics and Econometrics*, 1st ed., ser. Wiley Series in Probability and Statistics. Wiley, Feb. 2019.
- [42] T. Lee, P. M. Wensing, and F. C. Park, "Geometric Robot Dynamic Identification: A Convex Programming Approach," *IEEE Transactions on Robotics*, vol. 36, no. 2, pp. 348–365, Apr. 2020.
- [43] J. Radford and J. Burdick, "Local motion planning for nonholonomic control systems evolving on principal bundles," in *Proceedings of the International Symposium on Mathematical Theory of Networks and Systems (MTNS '98)*, Padova, Italy, Jul. 1998.
- [44] W. Magnus, "On the exponential solution of differential equations for a linear operator," *Communications on Pure and Applied Mathematics*, vol. 7, no. 4, pp. 649–673, Nov. 1954.
- [45] R. Hatton and H. Choset, "Nonconservativity and noncommutativity in locomotion: Geometric mechanics in minimum-perturbation coordinates," *The European Physical Journal Special Topics*, vol. 224, no. 17-18, pp. 3141–3174, Dec. 2015.
- [46] C. Bass, S. Ramasamy, and R. L. Hatton, "Characterizing error in non-commutative geometric gait analysis," in *2022 International Conference on Robotics and Automation (ICRA)*, May 2022, pp. 9845–9851.
- [47] A. Teel, R. Murray, and G. Walsh, "Nonholonomic control systems: From steering to stabilization with sinusoids," in *Proceedings of the 31st IEEE Conference on Decision and Control*. Tucson, AZ, USA: IEEE, 1992, pp. 1603–1609.
- [48] P. A. Vela, "Averaging and control of nonlinear systems," Ph.D. dissertation, California Institute of Technology, May 2003.
- [49] B. T. Hinson and K. A. Morgansen, "Observability-Based Optimal Sensor Placement for Flapping Airfoil Wake Estimation," *Journal of Guidance, Control, and Dynamics*, vol. 37, no. 5, pp. 1477–1486, Sep. 2014.
- [50] —, "Gyroscopic sensing in the wings of the hawkmoth *Manduca sexta*: The role of sensor location and directional sensitivity," *Bioinspiration & Biomimetics*, vol. 10, no. 5, p. 056013, Oct. 2015.
- [51] N. L. Brace, N. B. Andrews, J. Upsal, and K. A. Morgansen, "Sensor Placement on a Cantilever Beam Using Observability Gramians," in *2022 IEEE 61st Conference on Decision and Control (CDC)*. Cancun, Mexico: IEEE, Dec. 2022, pp. 388–395.
- [52] B. T. Hinson, M. K. Binder, and K. A. Morgansen, "Path planning to optimize observability in a planar uniform flow field," in *2013 American Control Conference*. Washington, DC: IEEE, Jun. 2013, pp. 1392–1399.
- [53] J. D. Quenzer and K. A. Morgansen, "Observability based control in range-only underwater vehicle localization," in *2014 American Control Conference*. Portland, OR, USA: IEEE, Jun. 2014, pp. 4702–4707.
- [54] Y. Yang, J. Khalife, J. J. Morales, and Z. M. Kassas, "UAV Waypoint Opportunistic Navigation in GNSS-Denied Environments," *IEEE Transactions on Aerospace and Electronic Systems*, vol. 58, no. 1, pp. 663–678, Feb. 2022.
- [55] B. Boyacioglu, D. Sandursky, and K. A. Morgansen, "Nonlinear Estimation of Rigid Body Inertial Parameters," in *AIAA SCITECH 2023 Forum*. National Harbor, MD & Online: American Institute of Aeronautics and Astronautics, Jan. 2023.
- [56] E. Sundquist, C. Whitehair, and K. A. Morgansen, "Nonlinear Multi-Sensor Observability and Estimation of Rigid Body Inertial Parameters," in *AIAA SCITECH 2024 Forum*. Orlando, FL: American Institute of Aeronautics and Astronautics, Jan. 2024.
- [57] A. P. Sabelhaus and C. Majidi, "Gaussian Process Dynamics Models for Soft Robots with Shape Memory Actuators," in *2021 IEEE 4th International Conference on Soft Robotics (RoboSoft)*. New Haven, CT, USA: IEEE, Apr. 2021, pp. 191–198.
- [58] D. Bruder, X. Fu, R. B. Gillespie, C. D. Remy, and R. Vasudevan, "Data-Driven Control of Soft Robots Using Koopman Operator Theory," *IEEE Transactions on Robotics*, vol. 37, no. 3, pp. 948–961, Jun. 2021.
- [59] Y. Yang and R. L. Hatton, "Geometric gait optimization for inertia-dominated systems with nonzero net momentum," in *2023 IEEE/RSJ International Conference on Intelligent Robots and Systems (IROS)*, Detroit, MI, USA, Oct. 2023, pp. 2877–2884.
- [60] A. Cabrera and R. L. Hatton, "Optimal control of robotic systems and biased Riemannian splines," *ESAIM: Control, Optimisation and Calculus of Variations*, vol. 30, p. 36, 2024.
- [61] J. Choi, A. Cabrera, and R. L. Hatton, "Geometric Optimal Control of Mechanical Systems with Gravitational and Resistive Force," Oct. 2024.
- [62] J. Choi, C. Bass, and R. L. Hatton, "Optimal gait families using lagrange multiplier method," in *2022 IEEE/RSJ International Conference on Intelligent Robots and Systems (IROS)*, Oct. 2022, pp. 8873–8878.
- [63] R. L. Hatton, R. A. Knepper, H. Choset, D. Rollinson, C. Gong, and E. Galceran, "Snakes on a plan: Toward combining planning and control," in *2013 IEEE International Conference on Robotics and Automation*. Karlsruhe, Germany: IEEE, May 2013, pp. 5174–5181.
- [64] A. Casal and M. H. Yim, "Self-reconfiguration planning for a class of modular robots," in *Photonics East '99*, G. T. McKee and P. S. Schenker, Eds., Boston, MA, Aug. 1999, pp. 246–257.